Crystal growth, characterization and electronic band structure of TiSeS

Y. Shemerliuk [1,*] A. Kuibarov [1] O. Feia [1,2] M. Behnami [1] H. Reichlova [1,3] O. Suvorov [1,4] S. Selter [1] D. V. Efremov [1]
S. Borisenko [1] B. Büchner [1,3] and S. Aswartham [1,†]

[1]*Institute for Solid State Research, Leibniz IFW Dresden, Helmholtzstr. 20, 01069 Dresden, Germany*
[2]*Kyiv Academic University, 03142, Kyiv, Ukraine*
[3]*Institute of Solid State and Materials Physics and Würzburg-Dresden Cluster of Excellence ct.qmat,
Technische Universität Dresden, 01062 Dresden, Germany*
[4]*G. V. Kurdyumov Institute for Metal Physics of the N.A.S. of Ukraine, 03142 Kyiv, Ukraine*

Layered semimetallic van der Waals material $TiSe_2$ has attracted a lot of attention because of interplay of a charge density wave (CDW) state and superconductivity. Its sister compound TiS_2, being isovalent to $TiSe_2$ and having the same crystal structure, shows a semiconducting behavior. The natural question rises—what happens at the transition point in $TiSe_{2-x}S_x$, which is expected for x close to one. Here we report the growth and characterization of TiSeS single crystals and the study of the electronic structure using density functional theory (DFT) and angle-resolved photoemission (ARPES). We show that TiSeS single crystals have the same morphology as $TiSe_2$. Transport measurements reveal a metallic state; no evidence of CDW was found. DFT calculations suggest that the electronic band structure in TiSeS is similar to that of $TiSe_2$, but the electron and hole pockets in TiSeS are much smaller. The ARPES results are in good agreement with the calculations.

I. INTRODUCTION

In recent years, research on functional two-dimensional (2D) materials has stimulated activities aimed at synthesizing new materials with novel functional properties. Due to their unique electronic [1–3], magnetic [4–6], and optical properties [7–9], the new 2D materials are expected to have great potential for applications. One of the most interesting classes is the transition metal dichalcogenides MX_2 (M = transition metal, X = chalcogenide). They and their mixed systems dominate among the current 2D materials due to their favorable structural [10,11], optical, electronic behavior [12–16].

MX_2 could be stabilized in a trigonal 1T, a hexagonal 2H, or a rhombohedral 3R structural phase. The electronic properties of MX_2 range from semiconductors [17] to semimetals [18–20], from material with a trivial electronic structure till topological semimetals [21] and topological insulators [22]. Due to these unique properties, MX_2 continue to attract the scientific community.

TiSeS is a member of the trigonal 2D MX_2 family with the space group of $P\bar{3}m1$ (No. 164), where Ti atoms are sandwiched between two layers of S and Se atoms and each TiSeS layer is bound by the van der Waals (vdW) interaction. Therefore, the individual layers can be easily exfoliated. One of two pristine compounds of the mixed crystal system $TiSe_{2-x}S_x$ ($0 \leqslant x \leqslant 2$) considered with x = 2 is a semiconductor with an indirect band gap, while another with x = 0 is a semimetal with slightly overlapping bands [23]. In $TiSe_2$ compounds, a charge density wave (CDW) transition is observed at about 200 K at ambient pressure [24,25]. $TiSe_2$ grown using high pressure shows insulating behavior at low temperatures [26]. However, Cu-intercalation or application of hydrostatic pressure suppress the CDW state, giving room for superconductivity [27,28]. It was shown that the maximum superconducting T_C corresponds to the CDW quantum critical point [29].

Motivated by this nontrivial behavior, in our work we try to use chemical pressure by substitution of Se by S to tune the material to the CDW quantum critical point. Since the ionic radius of S is smaller than Se, the substitution acts as an external pressure. As the first step, we optimized the synthesis and crystal growth conditions of TiSeS. Further, we have investigated the crystal structure, magnetic, and transport properties of as grown single crystals. Finally, we performed the band structure calculations using DFT and compare it with the ARPES measurements.

II. EXPERIMENTAL METHODS

The crystals were obtained from the Chemical Vapor Transport (CVT) crystal growth experiment. The chemical composition of our crystals was investigated using energy dispersive x-ray spectroscopy (EDX), with an accelerating voltage of 30 kV. Electron microscopic images were obtained by using a scanning electron microscope with two types of signals: the secondary electrons (SE) for topographic contrast and the backscattered electrons (BSE) for chemical contrast.

The crystal structure was investigated by powder x-ray diffraction (pXRD) using a STOE powder laboratory diffractometer in transmission geometry with Cu-K$_{\alpha1}$ radiation [the wavelength (λ) is 1.540560 Å] from a curved Ge (111)

---

single crystal monochromator and detected by a MYTHEN 1K 12.5° linear position sensitive detector manufactured by DECTRIS. An XRD pattern of a polycrystalline sample was obtained by grinding as-grown single crystals. Temperature and field dependent magnetization were measured on bulk as-grown crystal using a Quantum Design Superconducting Quantum Interference Device Vibrating Sample Magnetometer (SQUID-VSM). Transport measurements were carried on single crystals and the wires were glued by a conductive two component epoxy. Four contacts at the top surface (*ab* plane) and two contacts on the bottom surface of the sample were prepared to allow for a four probe method in both [in plane direction] and [*c* direction]. The measurements were performed in Oxford 15 T cryostat and the temperature was controlled by a heater at the sample holder. The electric current was applied either in the [*ab* plane] or [*c* direction]; longitudinal and transversal voltage was measured. Magnetic field was applied perpendicular to the *ab* plane for the charge carrier density measurements from Hall effect, and the transversal data were antisymmetrized prior the mobility evaluation. Several samples were prepared showing similar results. ARPES measurements of TiSeS were performed on the 1^2 station at BESSY synchrotron with the Scienta Omicron R8000 energy analyzer with total energy and momentum resolution less than 10 meV and 0.01 Å^{-1}, respectively. High quality single crystals were cleaved and measured in a chamber with pressure better than 8×10^{-11} mbar at a temperature less than 15 K.

Crystal Growth by Chemical Vapor Transport

TiSeS single crystals were grown by the chemical vapor transport technique. All preparation steps were performed under argon atmosphere in a glovebox before sealing the ampule. The starting materials titanium (powder, Alfa Aesar, 99.99%), selenium (pieces, Alfa Aesar, 99.97%), and sulfur (pieces, Alfa Aesar, 99.999%) were weighed out with a molar ratio of Ti : Se : S = 1 : 1 : 1 and homogenized in an agate mortar. 1 g of the starting material was loaded in a quartz ampule (10 mm inner diameter, 3 mm wall thickness) together with 0.04 g of the transport agent iodine. The filled ampule was cooled by liquid nitrogen, evacuated to a residual pressure of 10^{-8} bar and sealed at a length of approximately 12 cm by the oxy-hydrogen flame under static pressure.

The closed ampule was heated in a two-zone furnace with the following temperature profile optimized by us. Initially, the furnace was heated homogeneously to 790 °C with 100 °C/h. After that, an inverse transport gradient is applied to transport particles to the one side of the ampule which is the charge region. This region was kept at 790 °C for 336 h. The other side of the ampule, which is the sink region, was initially heated up to 840 °C at 100 °C/h, and dwelled at this temperature for 24 h. After that, the temperature in the growth zone was gradually reduced during one day to 730 °C to slowly form the transport temperature gradient for controlling nucleation and held at this temperature for 402 h. As a result, the temperature gradient was set for vapor transport between 790 °C (charge) and 730 °C (sink) for 17 days. Finally, the charge region was cooled to the sink temperature in two hours before both regions were furnace cooled to room temperature.
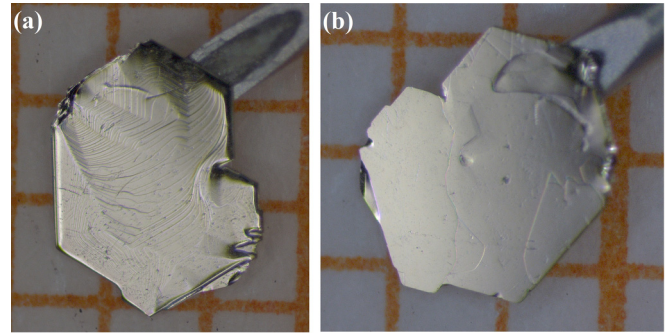

FIG. 1. (a) and (b) As-grown crystals of TiSeS by the chemical vapor transport, cell scale is 1 mm.

Thin lustrous platelike crystals of TiSeS perpendicular to the *c* axis in the size of approximately 3 mm × 3 mm × 100 μm were obtained. For example, as-grown single crystals are shown in Figs. 1(a) and 1(b). All of these crystals show a layered morphology and they are easily exfoliated by scotch tape.

III. CHARACTERIZATION: COMPOSITIONAL AND STRUCTURAL ANALYSIS

As-grown single crystals exhibit the typical features of layered systems, such as steps and terraces, as shown in Figs. 1(a) and 1(b). The topographical SE image of TiSeS crystal has a well-defined flat hexagonal facade with angles of 120°, which clearly indicates that they grew along the symmetry axes [Fig 2(a)]. The back scattered electron (BSE) image of our crystal has homogeneous chemical contrast over the surface of the crystal, as shown in Fig. 2(b). This indicates a homogeneous elemental composition on the respective area of the crystal. At some small areas, the observed contrast changes can be clearly attributed to some scratches on top of the crystal and not to compositional changes, as clearly seen by comparing with the SE image.

The elemental composition of the TiSeS single crystals was determined by energy-dispersive x-ray spectroscopy (EDX) via measuring different areas and points on the surface of the crystal. The compositional analysis of as-grown single crystals is Ti$_{34.4(1)}$Se$_{30.2(9)}$S$_{35.3(2)}$. The compound shows the expected composition within the error of this measurement technique. The result of EDX measurements highly depends
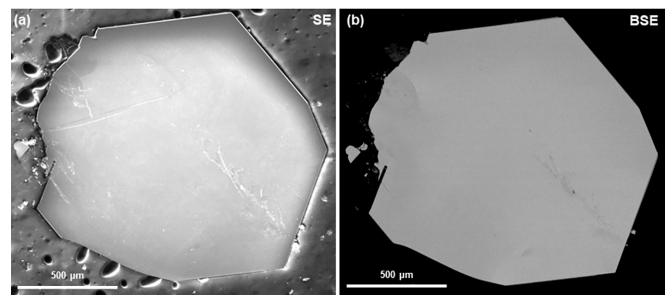

FIG. 2. SEM image of an as-grown TiSeS crystal with topographical contrast (SE mode) in (a) and chemical contrast (BSE mode) in (b).
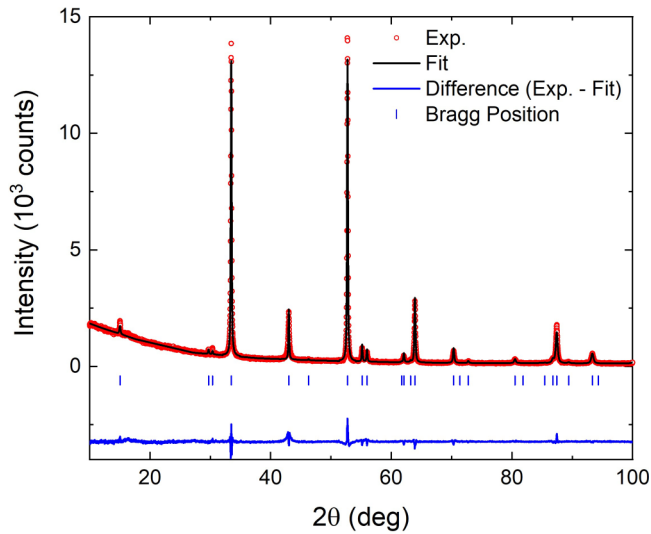
FIG. 3. Powder x-ray diffraction pattern together with the Rietveld analysis of TiSeS.

FIG. 4. As an example crystal structure of TiSeS (a) shown in the *bc* plane, (b) shown in the *ac* plane and (c) shown in the *ab* plane. The graphical representation was prepared using VESTA3 [33].

on the sample topography and the error regarding each element corresponds to an order of up to 5% [30].

The structural characterization and phase purity were confirmed by powder x-ray diffraction using a STOE powder diffractometer. The pXRD pattern obtained from TiSeS crystals, as shown in Fig. 3, was indexed in the space group $P\bar{3}m1$ (No. 164), in agreement with literature [31]. No additional reflections were observed demonstrating the phase purity of our crystals. Starting from the crystal structure model proposed by Bozorth [32], a refined crystal structure model is obtained using the Rietveld method.

Figure 3 shows x-ray pattern together with the calculated pattern based on the Rietveld analysis (black line), the difference between measured and calculated pattern (blue line), and the calculated Bragg positions for a trigonal unit cell. The calculated peak positions and intensities are in satisfactory agreement with the experimental data. TiSeS has a CdI_2-type structure with the titanium atom at (0, 0, 0) position and the chalcogen atoms at (1/3, 2/3, z) position with the random distribution of S and Se on a position as shown in Fig. 4. The obtained lattice parameters and reliability factors are summarized in Table I and the structure illustrated in Fig. 4.

IV. MAGNETIZATION AND TRANSPORT

A. Magnetic properties

The magnetic properties of the as-grown single crystals as well as polycrystalline samples of TiSeS were measured by SQUID-VSM. The measurements were performed both $H \parallel ab$ and $H \parallel c$. The magnetization as a function of temperature is shown in Fig. 5(a), the magnetization curve shows paramagneticlike behavior with slight negative values for $H \parallel ab$, which might be coming from excess amount of diamagnetic epoxy used to mount the crystal. To improve the measurement parameters and subsequent calculations, an additional measurement of the polycrystalline sample was made without the use of epoxy.
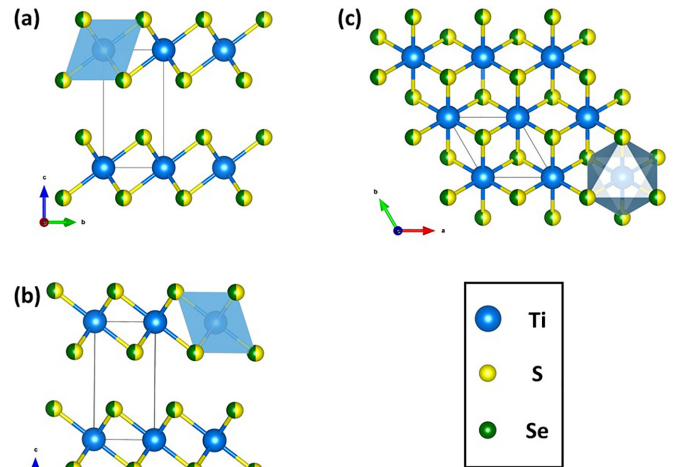
As shown in Fig. 5(b) the molar susceptibility as a function of temperature shows paramagnetic behavior without any long range order. Inverse susceptibility shown in Fig. 5(c) reveals that susceptibility becomes nonlinear below 250 K, i.e., paramagneticlike behavior is observed only at relatively high temperatures. Linear fit of the Curie-Weiss law results in $\theta_{CW} = -282$ K with an effective moment $\mu = 0.83\mu_B$, per unit cell. It indicates frustrated AFM-like interaction. At temperatures below 200 K we observe deviation from the Curie-Weiss law. The high effective moment has also been observed in the Ti-vacant samples in the $TiSe_2$ parent compound [34]. They concluded that localized spins of Ti at the interstitial positions or vacancies of Ti. Here we also observe similar high effective moments in TiSeS, most likely the localized moments of Ti are present. This is highly interesting as the localized spins can give interesting behavior such as spin glass and cluster

TABLE I. Structural parameters and residual factors of Rietveld refinement of TiSeS.

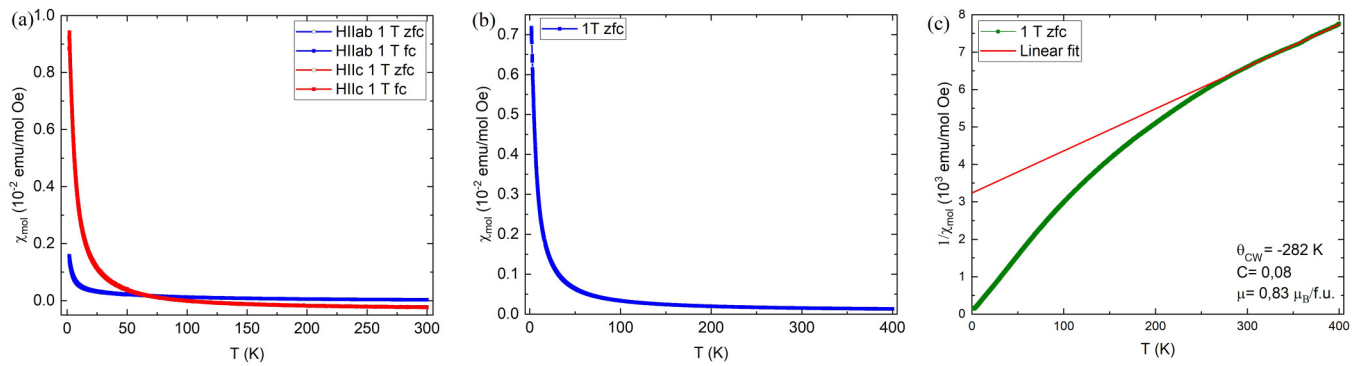| pXRD	
Composition	TiSeS
Space group	$P\bar{3}m1$ (No. 164)
Wavelength (A)	1.54059
Temperature (K)	293(2)
Radiation type	Cu-K$_{\alpha_1}$
Wavelength (A)	1.54059
2θ range (deg)	10-100
Step size (deg)	0.015
Temperature (K)	293(2)
a (A)	3.4681(8)
c (A)	5.879(3)
V (A^3)	61.243(3)
Goodness-of-fit	2.67
Bragg R-factor	6.372
RF-factor	6.967

FIG. 5. (a) Molar susceptibility as a function of temperature for a field of 1 T applied $H \parallel ab$ and $H \parallel c$ for TiSeS crystal. (b) Molar susceptibility as a function of temperature for a field of 1 T for TiSeS polycrystal. (c) Inverse molar susceptibility temperature dependence with Curie-Weiss linear fit.

glass [34–36]. In another recent work on [37], nonmagnetic system TiO_2 also exhibit large moments that can be caused by defects in the crystal structure.

B. Transport properties

Electrical resistivity measurement shows strongly anisotropic metallic behavior; $\rho_{xx} \sim T^n$ with $n = 1.7$ at low temperature. No indications of the critical fluctuations were observed down to 5 K suggesting that we are not in the QCP part of the phase diagram. The sheet resistivity is monotonously decreasing with temperature unlike [38]

showing metallike behavior in the studied temperature range [Fig. 6(a)]. The resistivity was measured with electrical current applied along various crystal directions: in the ab plane and in the c direction. The relative change of the resistivity with temperature is larger when electric current is applied in the ab plane pointing to the anisotropic transport properties arising from the van der Waals character of the material.

The magnetoresistance at various temperatures was measured at longitudinal contacts while sweeping magnetic field in the c direction as shown in Fig. 6(b). At low temperatures the magnetoresistance is increased reaching 0.3% at
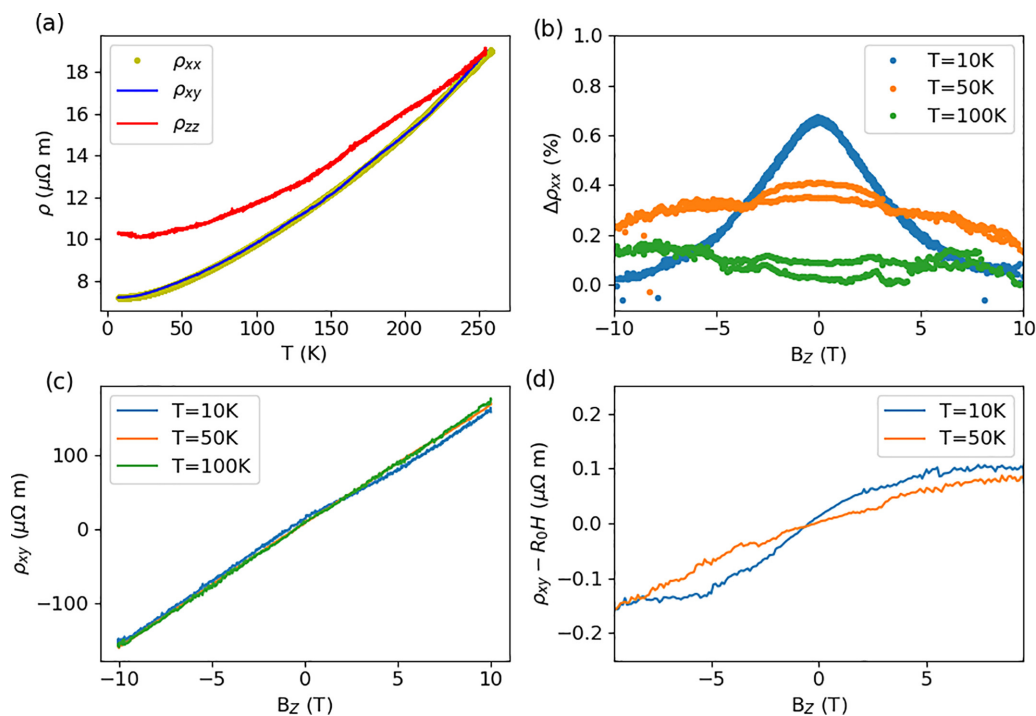

FIG. 6. Magneto-transport characterization of TiSeS single crystals. (a) Resistivity as a function of temperature for different crystal direction of the TiSeS single crystal. ρ_{xx} and ρ_{yy} were measured with electric current in the ab plane and the ρ_{zz} was measured with electric current applied along the c direction. (b) Magneto resistance measured at longitudinal contacts at various temperatures when magnetic field is applied along the c direction. (c) Hall measurements at various temperatures. (d) Linear slope was subtracted from the measured Hall signal to highlight the nonlinearity in magnetic field.

TABLE II. Structural parameters (in Angstrom) for Ti-Se-S system obtained with PBE pseudopotentials with and without disperse correction

Lattice constant	Experimental	PBE	PBE-D3(BJ)	PBE-D3(ZD)
		TiS_2		
a	3.407	3.409 ($\sim 0\%$)	3.368 (-1.14%)	3.400 (-0.21%)
c	5.695	6.487 ($+14.08\%$)	5.542 (-2.68%)	5.687 (-0.14%)
		TiSeS		
a	3.4681(8)	3.458 (-0.29%)	3.408 (-1.74%)	3.444 (-0.70%)
c	5.879(3)	6.743 ($+14.69\%$)	5.789 (-1.53%)	5.984 ($+1.78\%$)
		$TiSe_2$		
a	3.540	3.534 (-0.17%)	3.479 (-1.72%)	3.520 (-0.56%)
c	6.010	6.736 ($+12.08\%$)	5.895 (-1.91%)	6.065 ($+0.92\%$)

10 K. Interestingly, it deviates from the ordinary quadratic magnetoresistance and it has a negative character. It is probably caused by weak-localization effects due to the low dimensionality, as observed previously in van der Waals systems [39].

The carrier density concentration was estimated from the Hall effect [Fig. 6(c)] at various temperatures. The mobility at 10 K is 102 cm^2/V s and decreases at 100 K to 76 cm^2/V s. At low temperature a weak nonlinearity in the Hall data with respect to the magnetic field was observed. The magnetic field can influence the complex band structure of the material leading to such nonlinearity at high magnetic fields.

V. DFT-CALCULATION

Using *ab initio* calculations, we investigate the electronic band structure of $TiSe_2$, TiS_2, and TiSeS as well as the possible crystal structures. To investigate possible crystal structures of the new TiSeS crystal, we have performed an evolution search in conjunction with *ab initio* calculations in the frame of the density functional theory (DFT). For structure prediction of systems with mixed chalcogen composition we used USPEX code [40,41]. One can explore low-energy configurations for chosen composition with technique implemented in this code. To predict thermodynamic stability of the ternary crystals we used nonvariable search mode with minimum 12 atoms and maximum 18 atoms for 1st generations. It was produced by a random structure generator and consisted of 100 structures. Each of the following generations had eight compositions, which was obtained by applying 40% heredity, 20% softmutation, 10% lattice mutation, and 30% random structure generator. To check possible low-energy compositions we performed calculations for ternary stoichiometries within Ti, S, and Se atoms at ratio 1 : 1 : 1. Each structure was carefully relaxed in four stages, starting from low precision.

For structure relaxations within USPEX we used DFT [42] implemented in the VASP code [43,44]. Perdew-Burke-Ernzerhof (PBE), generalized gradient approximation (GGA) [45], and projector-augmented wave (PAW) [46,47] within DFT were used for these calculations. We have set the wave kinetic energy cutoff to 350 eV, and uniform Γ-centered k meshes with reciprocal-space resolution of $2\pi\,0.07\text{A}^{-1}$ were used for Brillouin zone sampling. In postprocessing we carefully relaxed all low-energy structures in USPEX output with $12 \times 12 \times 6$ k points mesh and energy cutoff 400 eV.

As the result of evolutionary search, we have got the set of low energy structures within Ti-Se-S system. The most stable structure has 156 point symmetry, and it consists of three different atom layers—Ti in the middle, while Se and S atoms are located on up and down layers. It is known that PBE approximation does not correctly treat van der Waals forces. To check if this material corresponds to experimental finding of this paper, we have applied dispersion correction to our computational finding with Becke-Jonson dumping PBE-D3(BJ) [48,49] and the Grimme zero dumping [49] PBE-D3(ZD). For comparison we have applied the same procedure to TiS_2 and $TiSe_2$ structures.

Experimental crystal structure for TiS_2 and $TiSe_2$ we collected from Springer Materials database. From Table II one can see the common GGA-PBE method overestimates the c lattice vector by 12–14% for all considered structures. While inclusion of dispersion correction gives more reasonable estimation by 1–2% difference with experimental results. Zero dumping method PBE-D3(ZD) gives the best fitness to experimental results with almost precise lattice constants length.

Unit cells of these structures expand in line from TiS_2 to $TiSe_2$ via TiSeS. As shown in Fig. 7 lattice vectors a and c for TiSeS lays on a line between parameters for TiS_2 and $TiSe_2$. This can be explained by changing the chalcogen's size followed with changing the structural constants.
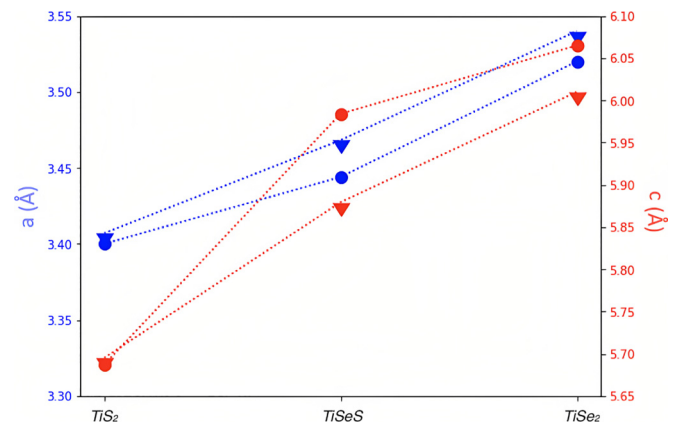

FIG. 7. Lattice constants for TiX_2 (X = S, Se) system, obtained with PBE in conjunction with zero dumping dispersion correction. Triangles stand for experimental data, circles are for calculated parameters.
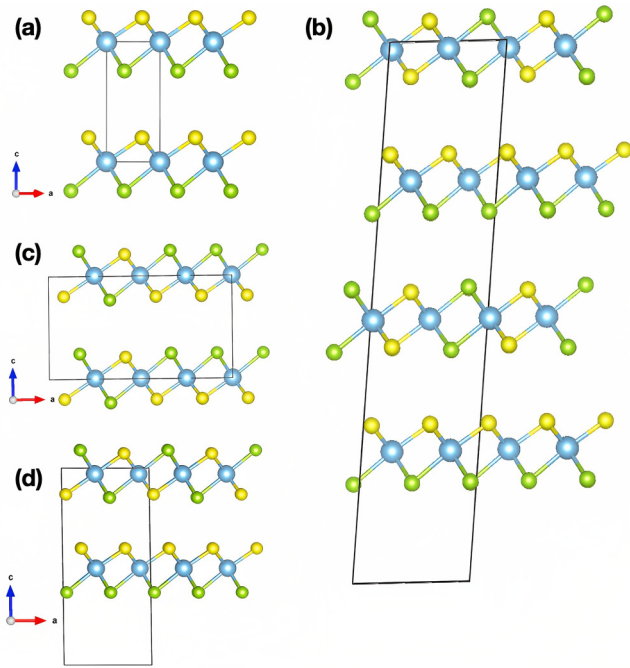
FIG. 8. Low energy Ti-Se-S structures, obtained with evolutionary search: (a) 156 symmetry, (b) 8 symmetry, (c) 1 symmetry, (d) 6 symmetry. Blue balls indicate Ti atoms, yellow and green are S and Se atoms, correspondingly.

Low energy structures, obtained by evolutionary search within PBE approximation, are presented on Fig. 8 and their structural parameters are collected in Table III. Here we present part of results for structures within 20 meV/f.u. (f.u. = formula unit) from material with 156 symmetry. All of them share structural similarity—they consist of trilayers with the Ti-layer as the central element, but with different arrangements of Si and S atoms. The most stable in our calculations is the structure with the crystal structure space group No. 156-TiSeS [Fig. 8(a)], which consists of three layers S-Ti-Se. Structure No. 8-TiSeS [Fig. 8(b)] with a huge unit cell with four trilayers shows some mixture of these atoms. It consists of S-Ti-Se trilayers, separated by trilayers with Se-S

TABLE III. Low energy Ti-Se-S structures, obtained with evolutionary search with PBE approximation—symmetry, lattice parameters, and energy difference per formula unit.

Symmetry	Structure constants (Å)	Angles	Energy difference (meV/f.u.)
156	$a = 3.458$	$\alpha = \beta = 90$	0
	$c = 6.740$	$\gamma = 120$	
8	$a = 3.470$	$\alpha = \gamma = 90$	14
	$b = 5.979$	$\beta = 95.204$	
	$c = 27.793$		
1	$a = 11.991$	$\alpha = 90.644$	15
	$b = 3.465$	$\beta = 89.926$	
	$c = 6.741$	$\gamma = 89.974$	
6	$a = 5.973$	$\alpha = \gamma = 90$	18
	$b = 3.465$	$\beta = 90.851$	
	$c = 13.392$		

composition. Similar structure shares No. 6-TiSeS [Fig. 8(d)], while No. 1-TiSeS [Fig. 8(d)] has one trilayer in the unit cell, but expanded a lattice constant. Along *a* its chalcogen layers consist of 1 Se (1 S) atom and 3 S (3 Se) atoms. While it is not possible in experimental conditions to achieve ideal composition, we believe there should be a mixture of different trilayers in grown crystals. As all discussed structures are close in energy, their mixture should result in 164 symmetry, which is observed in the experiment.

VI. ARPES

Measurements of TiSeS were performed on the 1^2 station at BESSY synchrotron with the Scienta Omicron R8000 energy analyzer with total energy and momentum resolution less than 10 meV and 0.01 A^{-1} respectively. High quality single crystals were cleaved and measured in a chamber with pressure better than 8×10^{-11} mbar at a temperature less than 15 K. ARPES spectra in Fig. 9 show that TiSeS hosts almost the same electronic structure as its parent compound—TiSe$_2$. Three holelike dispersions around the Γ-point and one electronlike pocket around the *M*-point. Measurements confirm previous statements in regard to the absence of commensurate charge density waves (CDW) [50] in TiSeS. There are no visible umklapp holelike bands near *M*-points. Figure 9(b) represents EDC taken at k$_{\parallel} = 0.5 \pm 0.02$ A^{-1} [red dashed line in Fig. 9(a)] and shows suppression of spectral weight around 0.14 eV binding energy (red arrow) visible in ARPES spectra which might be a sign of electron-phonon or electron-hole interaction that leads to formation of CDW in TiSe$_2$. In Fig. 9(d) the red arrow points to an additional, compared to TiSe$_2$, electron pocket in Γ-point which might be associated with the suppression of the CDW state in this compound. Its spectral weight is too weak compared to electron pockets in M; therefore, this band is almost not visible in the Fermi map in Fig. 9(c). Since the substitution of Se by S is isovalent, we performed the calculations for TiSe$_2$ and TiS$_2$ using the experimental structural parameters of TiSeS (Table I). The obtained band structures are shown in Fig. 9(e). The electronic structures of both compounds are similar to the electronic structure TiSeS in the coherent potential approximation (CPA) which is shown in Fig. 9(f). The calculation was done within the package FPLO [51,52]. In order to get a clue of the Fermi surface we calculate TiSe$_2$ with the structure parameters of TiSeS. The results are shown in Fig. 9(g). Comparison of ARPES [Fig. 9(c)] to the Fermi surface shows a good agreement.

VII. CONCLUSIONS

We report the growth and electronic structure characterization of TiSeS single crystals. TiSeS crystals exhibit a layered morphology with weak van der Waals interactions between layers parallel to the crystallographic *ab* plane of the trigonal structure in the space group $P\bar{3}m1$ (No. 164). Transport measurements show negative magneto resistance stemming from weak-localization effects. No indications of CDW were found in the transport. Our experiments were supplemented by the electronic band structure calculations in the frame of the density functional theory (DFT). Electronic band structure in TiSeS is similar to that in TiSe$_2$. The main difference is that the electron and hole pockets are much smaller in TiSeS. The
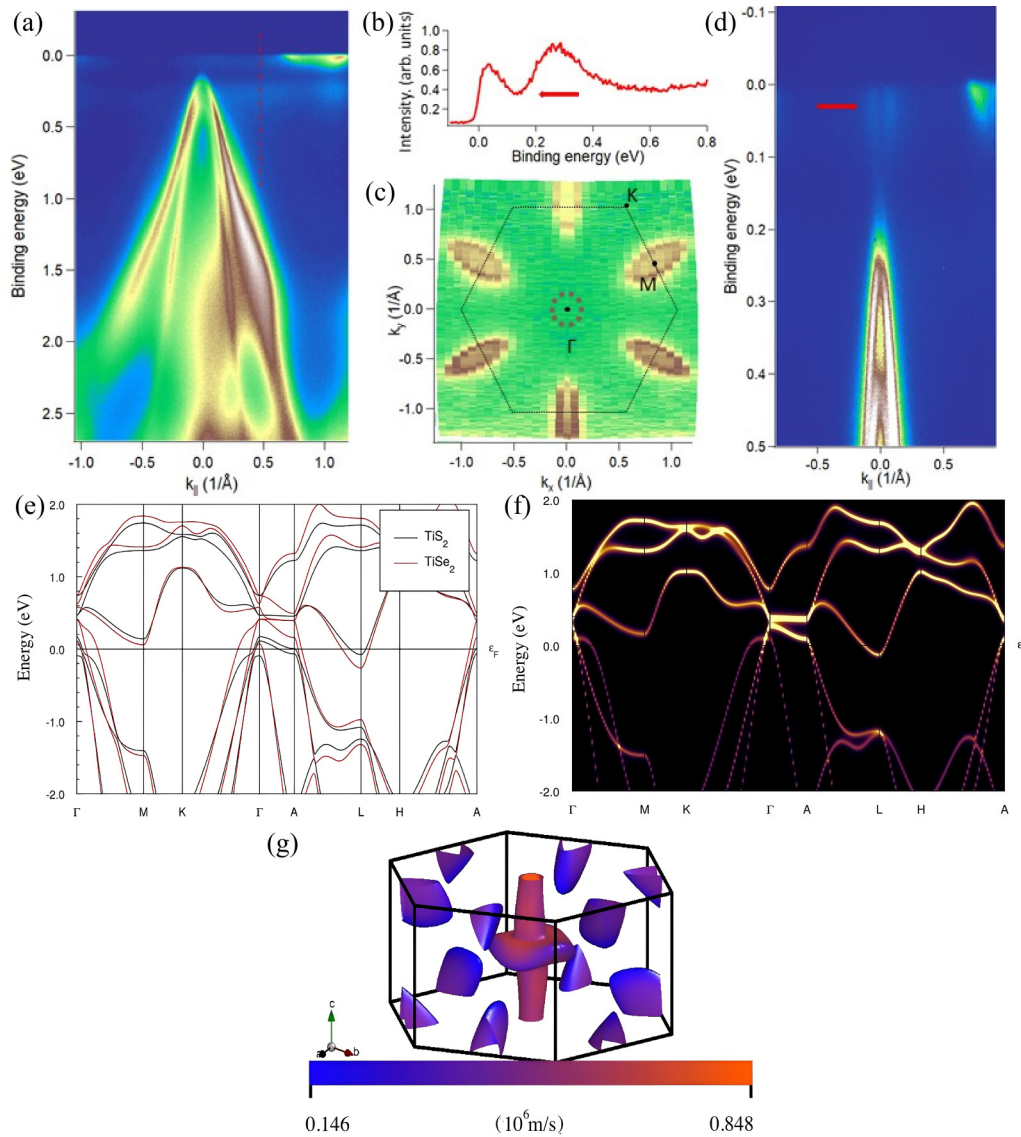
FIG. 9. ARPES spectra of TiSeS measured at 15 K along Γ-M direction using (a) 70 eV and (d) 35 eV photon energy. (b) Energy distribution curve (EDC) taken at $k_\parallel = 0.5$ A^{-1}. (c) Symmetrized Fermi surface map of TiSeS recorded with 80 eV photon energy. Brown dashed circle in center highlights electron pocket around Γ not clearly visible in the map due to strong intensity of electron pockets around M points. The electronlike pocket around Γ is clearly seen in panel (d) where we increase the dynamic range of the color scale enhancing the weak features. The dotted black hexagon represents the Brillouin zone. (e) Calculated band structure of experimental TiSe$_2$. (f) Band structure spectral function in CPA approximation for TiSeS. (g) Fermi surface of TiSe$_2$ with the structure parameters TiSeS; the color corresponds to the Fermi velocity

obtained band structure is confirmed in further angle-resolved photo emission (ARPES) experiments. We have studied band structure and low energy metastable states in the frame of the DFT theory. The lowest energy state is the one where the layers are three separate layers S-Ti-Se. However, there are many other low energy states. The "averaging" leads to the more symmetrical state No. 164 observed in the experiment.

[1] G. Fiori, F. Bonaccorso, G. Iannaccone, T. Palacios, D. Neumaier, A. Seabaugh, S. K. Banerjee, and L. Colombo, Electronics based on two-dimensional materials, Nat. Nanotechnol. **9**, 768 (2014).

[2] V. K. Sangwan and M. C. Hersam, Electronic transport in two-dimensional materials, Annu. Rev. Phys. Chem. **69**, 299 (2018).

[3] S. Kang, D. Lee, J. Kim, A. Capasso, H. S. Kang, J.-W. Park, C.-H. Lee, and G.-H. Lee, 2d semiconducting materials for electronic and optoelectronic applications: potential and challenge, 2D Mater. **7**, 022003 (2020).

[4] C. Gong, L. Li, Z. Li, H. Ji, A. Stern, Y. Xia, T. Cao, W. Bao, C. Wang, Y. Wang *et al.*, Discovery of intrinsic ferromagnetism in two-dimensional van der Waals crystals, Nature (London) **546**, 265 (2017).

[5] S. Selter, G. Bastien, A. U. B. Wolter, S. Aswartham, and B. Büchner, Magnetic anisotropy and low-field magnetic phase diagram of the quasi-two-dimensional ferromagnet $Cr_2Ge_2Te_6$, Phys. Rev. B **101**, 014440 (2020).

[6] M. A. McGuire, H. Dixit, V. R. Cooper, and B. C. Sales, Coupling of crystal structure and magnetism in the layered, ferromagnetic insulator CrI_3, Chem. Mater. **27**, 612 (2015).

[7] K. F. Mak and J. Shan, Photonics and optoelectronics of 2d semiconductor transition metal dichalcogenides, Nat. Photonics **10**, 216 (2016).

[8] F. Xia, H. Wang, D. Xiao, M. Dubey, and A. Ramasubramaniam, Two-dimensional material nanophotonics, Nat. Photonics **8**, 899 (2014).

[9] W. Zheng, Y. Jiang, X. Hu, H. Li, Z. Zeng, X. Wang, and A. Pan, Light emission properties of 2d transition metal dichalcogenides: Fundamentals and applications, Adv. Opt. Mater. **6**, 1800420 (2018).

[10] J. A. Wilson and A. Yoffe, The transition metal dichalcogenides discussion and interpretation of the observed optical, electrical and structural properties, Adv. Phys. **18**, 193 (1969).

[11] Z. Wei, B. Li, C. Xia, Y. Cui, J. He, J.-B. Xia, and J. Li, Various structures of 2d transition-metal dichalcogenides and their applications, Small Methods **2**, 1800094 (2018).

[12] J. He, K. Hummer, and C. Franchini, Stacking effects on the electronic and optical properties of bilayer transition metal dichalcogenides MoS_2, $MoSe_2$, WS_2, and WSe_2, Phys. Rev. B **89**, 075409 (2014).

[13] H.-L. Liu, C.-C. Shen, S.-H. Su, C.-L. Hsu, M.-Y. Li, and L.-J. Li, Optical properties of monolayer transition metal dichalcogenides probed by spectroscopic ellipsometry, Appl. Phys. Lett. **105**, 201905 (2014).

[14] A. Kuc, T. Heine, and A. Kis, Electronic properties of transition-metal dichalcogenides, MRS Bull. **40**, 577 (2015).

[15] R. Roldán, J. A. Silva-Guillén, M. P. López-Sancho, F. Guinea, E. Cappelluti, and P. Ordejón, Electronic properties of single-layer and multilayer transition metal dichalcogenides MX_2 (M=Mo, W and X=S, Se), Annalen der Physik **526**, 347 (2014).

[16] X. Tian, D. S. Kim, S. Yang, C. J. Ciccarino, Y. Gong, Y. Yang, Y. Yang, B. Duschatko, Y. Yuan, P. M. Ajayan *et al.*, Correlating the three-dimensional atomic defects and electronic properties of two-dimensional transition metal dichalcogenides, Nat. Mater. **19**, 867 (2020).

[17] X. Duan, C. Wang, A. Pan, R. Yu, and X. Duan, Two-dimensional transition metal dichalcogenides as atomically thin semiconductors: Opportunities and challenges, Chem. Soc. Rev. **44**, 8859 (2015).

[18] M. Ezawa, Second-order topological insulators and loop-nodal semimetals in transition metal dichalcogenides XTe_2 (M=Mo, W), Sci. Rep. **9**, 5286 (2019).

[19] A. H. Castro Neto, Charge Density Wave, Superconductivity, and Anomalous Metallic Behavior in 2D Transition Metal Dichalcogenides, Phys. Rev. Lett. **86**, 4382 (2001).

[20] Y.-T. Hsu, A. Vaezi, M. H. Fischer, and E.-A. Kim, Topological superconductivity in monolayer transition metal dichalcogenides, Nat. Commun. **8**, 14985 (2017).

[21] Y. Qi, P. G. Naumov, M. N. Ali, C. R. Rajamathi, W. Schnelle, O. Barkalov, M. Hanfland, S.-C. Wu, C. Shekhar, Y. Sun *et al.*, Superconductivity in Weyl semimetal candidate $MoTe_2$, Nat. Commun. **7**, 11038 (2016).

[22] Y. Ma, L. Kou, B. Huang, Y. Dai, and T. Heine, Two-dimensional ferroelastic topological insulators in single-layer Janus transition metal dichalcogenides MSSe (M=Mo, W), Phys. Rev. B **98**, 085420 (2018).

[23] J. A. Wilson, Concerning the semimetallic characters of TiS_2 and $TiSe_2$, Solid State Commun. **22**, 551 (1977).

[24] A. Wegner, J. Zhao, J. Li, J. Yang, A. A. Anikin, G. Karapetrov, K. Esfarjani, D. Louca, and U. Chatterjee, Evidence for pseudo–Jahn-Teller distortions in the charge density wave phase of 1T-$TiSe_2$, Phys. Rev. B **101**, 195145 (2020).

[25] A. J. Li, X. Zhu, D. Rhodes, C. C. Samouce, L. Balicas, and A. F. Hebard, Van der Waals Schottky barriers as interface probes of the correlation between chemical potential shifts and charge density wave formation in 1T-$TiSe_2$ and 2H-$NbSe_2$, Phys. Rev. B **96**, 125301 (2017).

[26] D. J. Campbell, C. Eckberg, P. Y. Zavalij, H.-H. Kung, E. Razzoli, M. Michiardi, C. Jozwiak, A. Bostwick, E. Rotenberg, A. Damascelli *et al.*, Intrinsic insulating ground state in transition metal dichalcogenide $TiSe_2$, Phys. Rev. Mater. **3**, 053402 (2019).

[27] A. F. Kusmartseva, B. Sipos, H. Berger, L. Forro, and E. Tutiš, Pressure Induced Superconductivity in Pristine 1T-$TiSe_2$, Phys. Rev. Lett. **103**, 236401 (2009).

[28] G. Wu, H. X. Yang, L. Zhao, X. G. Luo, T. Wu, G. Y. Wang, and X. H. Chen, Transport properties of single-crystalline Cu_xTiSe_2 ($0.015 \leqslant x \leqslant 0.110$), Phys. Rev. B **76**, 024513 (2007).

[29] T.-H. Park, O. P. Uzoh, and H.-Y. Choi, Maximal superconductivity in proximity to the charge density wave quantum critical point in Cu_xTiSe_2, Phys. Rev. B **104**, 184506 (2021).

[30] J. I. Goldstein, D. E. Newbury, P. Echlin, D. C. Joy, C. E. Lyman, E. Lifshin, L. Sawyer, J. R. Michael, J. I. Goldstein, D. E. Newbury *et al.*, Special topics in scanning electron microscopy, Scanning Electron Microscopy and X-ray Microanalysis: Third Edition, 195 (2003).

[31] H. Rimmington and A. Balchin, The growth by iodine vapour transport techniques and the crystal structures of layer compounds in the series TiS_xSe_{2-x}, TiS_xTe_{2-x}, $TiSe_xTe_{2-x}$, J. Cryst. Growth **21**, 171 (1974).

[32] R. M. Bozorth, The crystal structure of cadmium iodide, J. Am. Chem. Soc. **44**, 2232 (1922).

[33] A. H. Larsen, J. J. Mortensen, J. Blomqvist, I. E. Castelli, R. Christensen, M. Dułak, J. Friis, M. N. Groves, B. Hammer, C. Hargus *et al.*, The atomic simulation environment—a Python library for working with atoms, J. Phys.: Condens. Matter **29**, 273002 (2017).

[34] M. Sasaki, A. Ohnishi, T. Kikuchi, M. Kitaura, K. Shimada, and H.-J. Kim, Anomalous transport properties in fe intercalation compound $Fe_x TiSe_2$ single crystals, J. Low Temp. Phys. **161**, 375 (2010).

[35] H. Negishi, A. Shoube, H. Takahashi, Y. Ueda, M. Sasaki, and M. Inoue, Magnetic properties of intercalation compounds $M_x TiS_2$ (M=3d transition metal), J. Magn. Magn. Mater. **67**, 179 (1987).

[36] H. Negishi, K. Sadahiro, S. Ōhara, M. Koyano, M. Sasaki, and M. Inoue, Spin-glass behavior in itinerant magnetic material of $Fe_x TiS_2$, J. Magn. Magn. Mater. **90-91**, 345 (1990).

[37] M. Stiller and P. D. Esquinazi, Defect-induced magnetism in TiO_2: An example of quasi 2d magnetic order with perpendicular anisotropy, Front. Phys. **11**, 1124924 (2023).

[38] L. Li, E. O'Farrell, K. Loh, G. Eda, B. Özyilmaz, and A. Castro Neto, Controlling many-body states by the electric-field effect in a two-dimensional material, Nature (London) **529**, 185 (2016).

[39] G. Zheng, N. Wang, J. Yang, W. Wang, H. Du, W. Ning, Z. Yang, H.-Z. Lu, Y. Zhang, and M. Tian, Weak localization effect in topological insulator micro flakes grown on insulating ferrimagnet $BaFe_{12}O_{19}$, Sci. Rep. **6**, 21334 (2016).

[40] A. R. Oganov and C. W. Glass, Crystal structure prediction using *ab initio* evolutionary techniques: Principles and applications, J. Chem. Phys. **124**, 244704 (2006).

[41] A. R. Oganov, A. O. Lyakhov, and M. Valle, How evolutionary crystal structure prediction works and why, Acc. Chem. Res. **44**, 227 (2011).

[42] P. Hohenberg and W. Kohn, Inhomogeneous electron gas, Phys. Rev. **136**, B864 (1964).

[43] G. Kresse and J. Hafner, *Ab initio* molecular dynamics for open-shell transition metals, Phys. Rev. B **48**, 13115 (1993).

[44] G. Kresse and J. Furthmüller, Efficient iterative schemes for *ab initio* total-energy calculations using a plane-wave basis set, Phys. Rev. B **54**, 11169 (1996).

[45] J. P. Perdew, K. Burke, and M. Ernzerhof, Generalized Gradient Approximation Made Simple, Phys. Rev. Lett. **77**, 3865 (1996).

[46] P. E. Blöchl, Projector augmented-wave method, Phys. Rev. B **50**, 17953 (1994).

[47] G. Kresse and D. Joubert, From ultrasoft pseudopotentials to the projector augmented-wave method, Phys. Rev. B **59**, 1758 (1999).

[48] S. Grimme, S. Ehrlich, and L. Goerigk, Effect of the damping function in dispersion corrected density functional theory, J. Comput. Chem. **32**, 1456 (2011).

[49] S. Grimme, J. Antony, S. Ehrlich, and H. Krieg, A consistent and accurate *ab initio* parametrization of density functional dispersion correction (DFT-D) for the 94 elements H-Pu, J. Chem. Phys. **132**, 154104 (2010).

[50] M.-L. Mottas, T. Jaouen, B. Hildebrand, M. Rumo, F. Vanini, E. Razzoli, E. Giannini, C. Barreteau, D. R. Bowler, C. Monney, H. Beck, and P. Aebi, Semimetal-to-semiconductor transition and charge-density-wave suppression in 1T- $TiSe_{2-x}S_x$ single crystals, Phys. Rev. B **99**, 155103 (2019).

[51] http://www.fplo.de.

[52] K. Koepernik and H. Eschrig, Full-potential nonorthogonal local-orbital minimum-basis band-structure scheme, Phys. Rev. B **59**, 1743 (1999).